Prediction and analysis of combustion instabilities in a model rocket engine

Laurent Selle, Rodolphe Blouquin, Marie Théron, Luc-Henry Dorey, Martin Schmid, William Anderson

Prediction and analysis of combustion instabilities in a model rocket engine

Laurent Selle[1]
CNRS; IMFT; F-31400 Toulouse, France

Onera - The French Aerospace Lab, F-92322 Châtillon, France

Rodolphe Blouquin[2]
Bertin Technologies, F-78180, Montigny-le-Bretonneux, France

Marie Théron[3]
CNES, F-75612 Paris, France

Luc-Henry Dorey[4]
Onera - The French Aerospace Lab, F-92322 Châtillon, France

Martin Schmid[5]
Technische Universität München, D-85748 Garching Germany

William Anderson[6]
Purdue University, West Lafayette, Indiana 47907

[1] CNRS Research Fellow, IMFT, Allée Camille Soula, F-31400 Toulouse, France.
[2] Engineer, BCM/SIMA, 10 bis, avenue Ampère, 78180, Montigny-le-Bretonneux.
[3] Combustion Devices Specialist - DLA/SDT/EPM, 52 rue Jacques Hillairet, 75612 Paris Cedex, France.
[4] Research Engineer, DEFA, 29 avenue de la Division Leclerc, 92322 Chatillon Cedex, France.
[5] PhD Student, Lehrstuhl für Thermodynamik, Technische Universität München Boltzmannstr. 15, D-85748 Garching Germany.
[6] Professor, School of Aeronautics and Astronautics. Purdue University, 701 W. Stadium Ave. West Lafayette, IN 47907-2045. Associate Fellow AIAA.

This paper is a compilation of the research efforts of five different groups (Bertin Technologies and CNES, IMFT, ONERA, Purdue University and Technische Universität München) on the prediction of combustion instabilities in a model rocket engine. This research was initiated by the REST group (Rocket Engine Stability iniTiative) for the *2nd REST Workshop on Combustion Instability Modeling*, **which took place in October 2010 at Astrium GmbH in Ottobrunn. The target experiment consists of a single shear coaxial injector using methane and decomposed hydrogen peroxide as reactants. Both the inlet of the injector and the outlet of the chamber are choked, resulting in well-defined acoustic boundary conditions. The length of the oxidizer tube could be varied continuously and its influence on the stability is studied. Many numerical strategies were tested, addressing different physical phenomena at play during unstable combustion. Acoustic solvers, both with and without mean-flow effects were used to draw stability maps. The weak spot of these solvers is that they require the flame response to acoustic perturbations as an input. Large-Eddy Simulations, requiring no such a priori knowledge, were performed with the intent to elucidate flame stabilization and flame response mechanisms.**

Nomenclature

D_{ch} = combustion chamber diameter [cm]

D_{inj} = injector outlet diameter [cm]

D_{no} = outlet nozzle throat diameter [cm]

D_{op} = oxidizer post diameter [cm]

H_{slit} = fuel-slit height [mm]

$H_{splitter}$ = oxidizer/fuel splitter height [mm]

L_{ch} = combustion chamber length [cm]

L_{op} = oxidizer post length [cm] or [in]

M_{ch} = mean Mach number in the combustion chamber

M_{ox} = mean Mach number in the oxidizer-post length

$\dot{m}_f$ = fuel mass-flow rate [kg.s^{-1}]

$\dot{m}_{ox}$ = oxidizer mass-flow rate [kg.s^{-1}]

T_{ox} = oxidizer inlet temperature [K]

Z = acoustic impedance

ϕ = equivalence ratio

λ = acoustic CFL number

I. Introduction

A combustion instability results from the constructive coupling between unsteady heat release rate and acoustic waves. If the fraction of the power of the flame that feeds acoustics exceeds the acoustic losses (fluxes at the boundaries, transfer to vorticity, viscous dissipation, etc.) then an instability develops. Because of the large power density available in most combustion applications, a small fraction of this power is sufficient to generate large pressure fluctuations, which can rapidly cause mechanical failure. A necessary condition for a combustion instability to occur was first enunciated by Rayleigh [1], however, a wide variety of physical phenomena may be at play so that the prediction of the stability of an engine remains beyond current capabilities.

Since the early days of rocket science, the development of propulsion systems has been plagued

with combustion instabilities. It was only through a very costly trial and error process that rockets were flown. In the words of Hawthorne [2], in these days '*No one designs an injector plate with its multitude of small holes, they develop it.*' To some extent, this statement may still hold today. The seminal work of Crocco and Cheng [3] lays the basis of a theoretical framework to treat combustion instabilities, but this is still a very active research field [4–6] and no complete theory is yet available.

With the advent of three-dimensional unsteady computational fluid dynamics (CFD), the understanding of the key physical mechanisms involved in the unstable loop has made considerable progress. The increase in computational resources now suggests that CFD may also be a viable design and pre-test tool at a cost much lower than experiments. However, there is a need for validation on laboratory-scale experiments. The objective of the present paper is to assess the capability of various solvers and strategies to predict the stability map of a model rocket engine.

This research was initiated for the 2^{nd} *REST Workshop on Combustion Instability Modeling*, which took place in October 2010 at Astrium GmbH in Ottobrunn. The members of the REST group (Rocket Engine Stability iniTiative) are concerned with the study of combustion instabilities in rocket engines. It is a cooperation between French and German institutions and universities, sharing their knowledge on combustion instabilities. The goal of the workshop was to make available experimental data on an unstable model rocket engine installed at Purdue University and invite contributions on the numerical simulation of this experiment.

The burner and operating conditions are presented in Sec. II, followed by the main experimental results in Sec. III. Section IV describes the four sets of numerical simulations provided by the contributors to the workshop: Bertin Technologies and CNES, IMFT, ONERA and Technische Universität München.

II. Description of the experimental setup

A. Apparatus

The benchmark for this study on the numerical simulation of combustion instabilities in a model rocket combustor is an experimental setup designed and operated at Purdue University (Indiana, USA) [7–9], presented in Fig. 1. It consists of a cylindrical combustion chamber (diameter

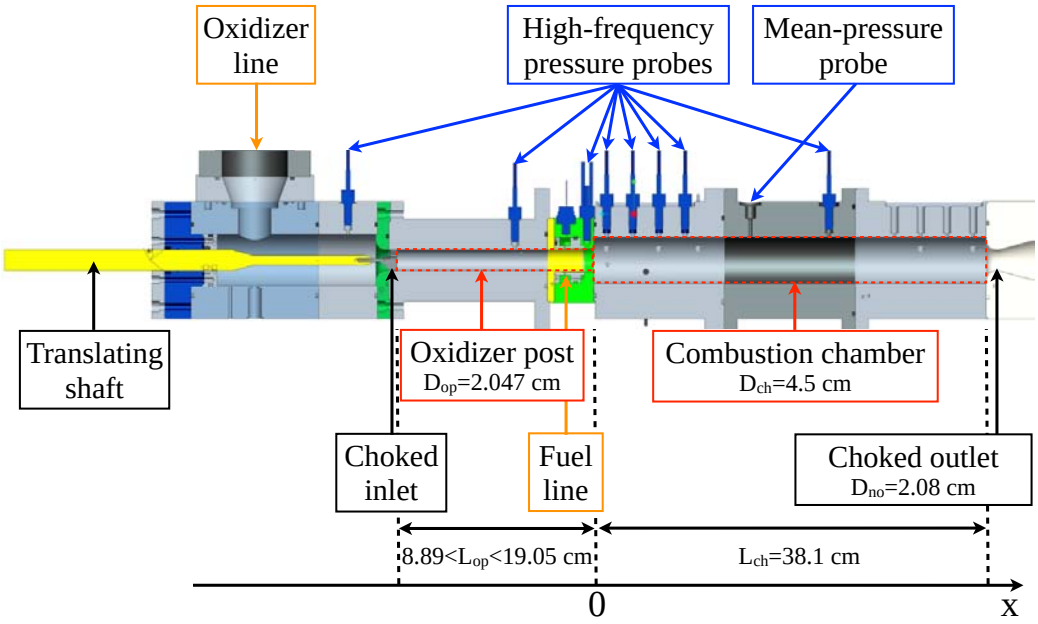

Fig. 1 Longitudinal cut of the CVRC experiment operated at Purdue University.

D_{ch} = 4.5 cm and length L_{ch} = 38.1 cm) with a single coaxial injector (outlet diameter D_{inj} = 2.306 cm), closed by a nozzle (throat diameter D_{no} = 2.08 cm). The inner section of the injector (diameter D_{op} = 2.047 cm) feeds the chamber with oxidizer while the outer slit (height H_{slit} = 0.406 mm) injects the fuel. The thickness of the material that separates the two streams of reactants is $H_{splitter}$ = 0.889 mm and the whole geometry is fully axisymmetric (*cf.* Fig. 2(a)). The fuel is fed into the axisymmetric slit by 36 holes, equally spaced circumferentially, that are choked under normal operating conditions. This setup is called Continuously Variable Resonance Chamber (CVRC) because the choked section at the entrance of the oxidizer post (*cf.* Fig. 2(b)) is mounted on a translating shaft, thus imposing a well defined variable acoustic length, L_{op}, for the injector. This length can be varied from 8.89 cm (3.5 in) to 19.05 cm (7.5 in), with respect to the inlet of the combustion chamber. The apparatus is equipped with a mean pressure probe, in order to determine operating conditions, as well as a number of high-frequency dynamic pressure sensors for the study of acoustics. The most upstream dynamic sensor in the combustion chamber is located 1.27 cm downstream of the injector face and is referred to as P_2 in this paper.

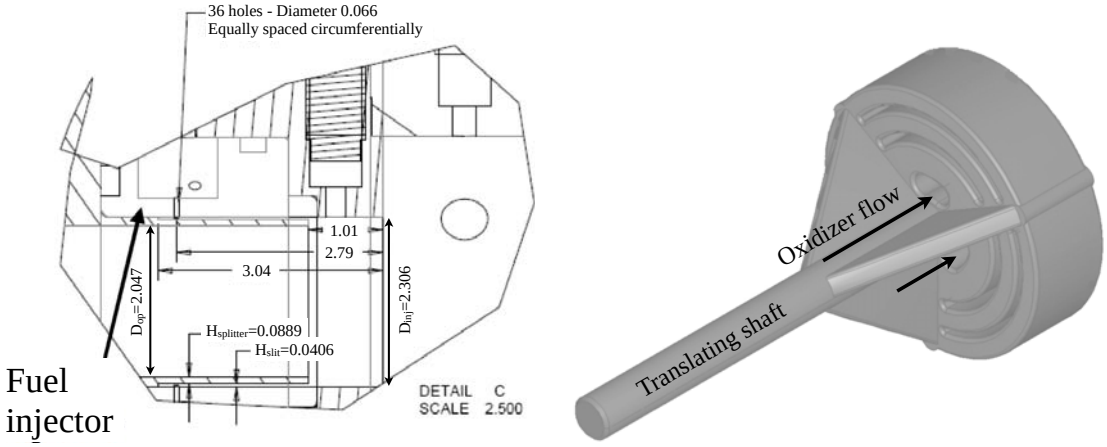

(a) Zoom on the fuel line. Dimensions in cm.

(b) Choked oxidizer injector inlet.

Fig. 2 Details of the fuel and oxidizer feeding lines.

B. Operating conditions

The fuel is pure gaseous methane. The oxidizer is a mixture of 90 % hydrogen peroxide and 10 % water, which are fully decomposed: this is equivalent to 42 % oxygen and 58 % water (per mass unit). The oxidizer is injected in the chamber at $T_{ox} = 1030$ K so that both water and oxygen are in gaseous phase. The operating point considered in this work is presented in Tab. 1. For these conditions, the whole range of oxidizer-post length L_{op} is explored and the corresponding stability maps is determined.

Table 1 Operating conditions for the CVRC.

Oxidizer flow rate ($\dot{m}_{ox}$)	[kg.s^{-1}]	0.32
Fuel flow rate ($\dot{m}_f$)	[kg.s^{-1}]	0.027
Global equivalence ratio (ϕ)		0.8
Oxidizer manifold pressure	[MPa]	4.48
Fuel manifold pressure	[MPa]	1.79
Oxidizer-post length range (L_{op})	[cm]	8.89 - 19.05
Mean chamber pressure	[MPa]	1.34

III. Experimental results

A typical run of the experiment is conducted with the following procedure:

- Five seconds into the sequence ($t = 5$ s), the oxidizer valve is fully opened.
- At $t = 8.5$ s, the fuel valve is opened. First a slug of JP-8 (25 mL) flows from the fuel manifold resulting in autoignition around $t = 8.7$ s.
- JP-8 is rapidly flushed out by methane and once ignition transients have passed, the traversing mechanism is actuated at $t = 9.5$ s. The oxidizer injector moves 10.2 cm in 2.0 s.
- Fuel is shut off at $t = 11.5$ s, followed by oxidizer at $t = 14$ s.

A typical pressure trace, recorded at the inlet to the converging throat ($x = 36.8$ cm) is presented in Fig. 3(a), together with the measured evolution of L_{op}. The raw data is first high-pass filtered

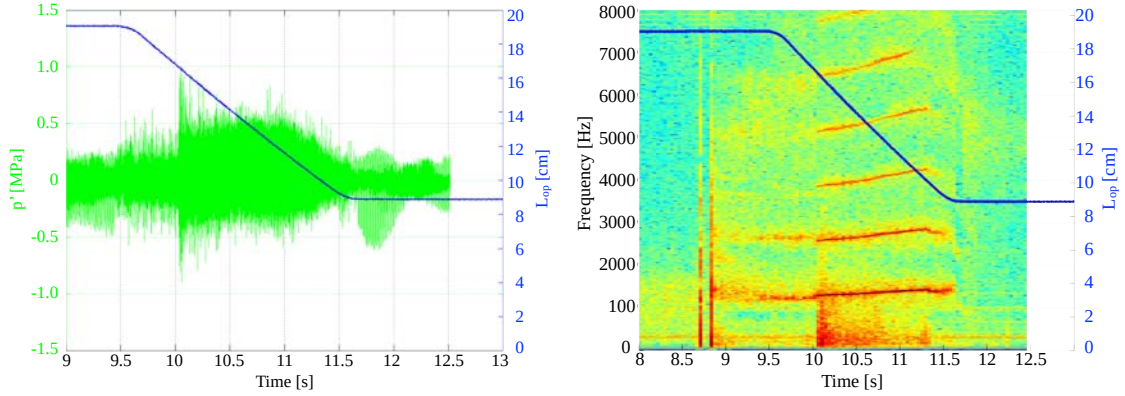

(a) High-pass filtered pressure trace.

(b) Spectrogram.

Fig. 3 Analysis of the dynamic pressure signal recorded at $x = 36.8$ cm during a typical run at variable L_{op}. The blue line represents the measured evolution of L_{op}.

at 150 Hz to eliminate electronic noise at 60 and 120 Hz. The high-pass filtered data reflects the peak-to-peak pressure fluctuations with respect to time, showing the combined effects from all the unstable frequencies. It indicates how transitions between linear and nonlinear stability regimes occur as the acoustic properties of the CVRC system vary with L_{op}. A large pressure spike can be seen at the onset of instability, at about $t = 10.1$ s. High-amplitude oscillations remain until about $t = 11$ s, when they begin to damp out. The apparently large oscillations past $t = 11.5$ s are due to nitrogen purge through the fuel system during shutdown..

Figure 3(b) is a sample spectrogram using the measured dynamic pressure of Fig. 3(a). Spectrograms are two-dimensional representations of the pressure power spectral density (PSD) of each

mode in time and used to illustrate the combustor response to the continuously variable acoustic eignenmodes. Signal powers are represented using the color scale –red and blue for high and low signal power, respectively– which remains consistent in time. In this test, the translating shaft of Fig. 2(b) is pushed forward, corresponding to a reduction of L_{op}. As expected, the frequency varies inversely with L_{op}. Relative stability is observed at $L_{op} = 19.1$ cm with two weak unstable modes near 1400 Hz and 2800 Hz. Once L_{op} shortens to about 16.8 cm (*i.e.* $t = 10.1$ s), the system transitions into a highly unstable regime, with distinct sharpening of the lowest two modes and a near-instantaneous appearance of higher-order harmonics. This highly unstable condition is sustained through $L_{op} = 12.1$ cm. As the tube length is reduced, the system transitions back to a relatively stable regime. Unlike the instantaneous and simultaneous appearance of the higher harmonics when the system transitions to the highly unstable regime, when the system transitions to a more stable condition, the higher harmonics disappear sequentially, led by the highest order.

A. Stability map

Three types of tests were conducted: forward translating tests (as shown in Fig. 3), backward translating tests, and tests where the oxidizer post length is fixed. The forward and backward tests are used to determine potential hysteresis effects and to check repeatability. The fixed post tests are used to check the quasi-steady-state approximation, *e.g.* how the limit-cycle amplitudes are affected by the translation. A comparison between these tests is shown in Fig. 4, where the measured PSD of the first mode is plotted as a function of L_{op}. The stability map confirms the interpretation of Fig. 3(b) that is the experiment exhibits a wide unstable range for intermediate values of L_{op}, bounded by two stable zones. It can also be seen that the repeatability is very good for low values of L_{op}. Considerable variability occurs with the longer post lengths, suggesting different controlling mechanisms on either side of the stability boundary. The highest amplitude pressure oscillations occur near $L_{op} = 12$ cm.

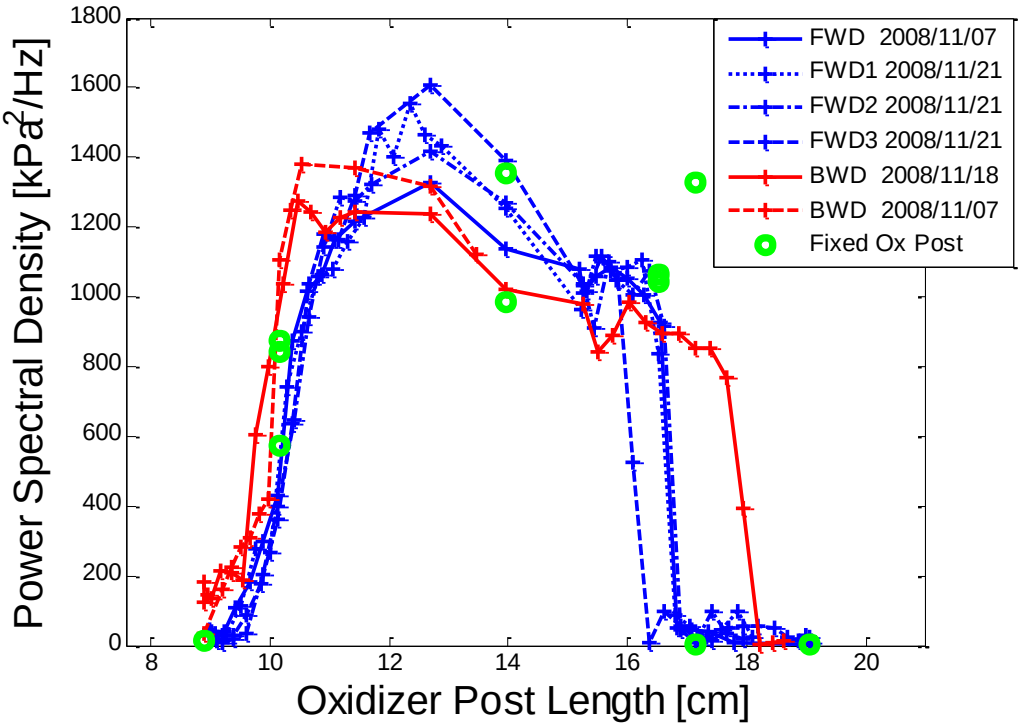

Fig. 4 Stability map of the CVRC experiment: power spectral density of the first mode versus L_{op}. The oxidizer translating shaft is either pushed forward, pulled backward or kept at a fixed position during the test.

B. Analysis of selected operating conditions

Four operating conditions are chosen for detailed analysis. The values of L_{op} together with the frequency and growth rate of the most unstable mode are given in Tab. 2.

Table 2 Selected values of L_{op} for detailed analysis. Frequency, amplitude and growth rate of the most unstable mode. Amplitudes are computed from the PSDs using the full-width, half-maximum approach.

Name	L_{op} [cm] / [in]	Frequency [Hz]	Amplitude [kPa]	Growth rate [s^{-1}]
Case A	19.05 / 7.5	1215	40.3	134
Case B	16.76 / 6.6	1282	337	199
Case C	11.43 / 4.5	1392	463	344
Case D	9.53 / 3.75	1379	68.3	180

The PSD of the pressure signal at point P_2 is presented in Fig. 5 for the four selected cases. The

spectra are obtained from signals of 0.1 s and assuming the quasi-steadiness of the instability. For

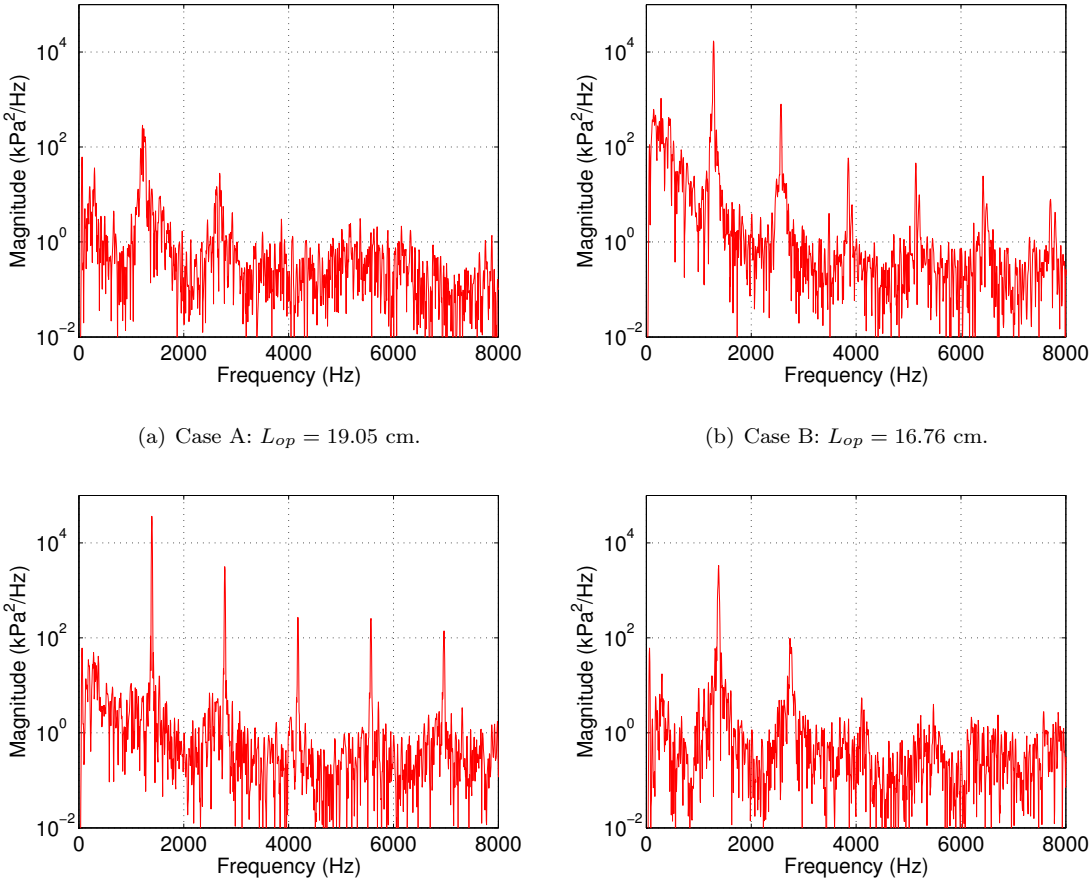

(a) Case A: $L_{op} = 19.05$ cm.

(b) Case B: $L_{op} = 16.76$ cm.

(c) Case C: $L_{op} = 11.43$ cm.

(d) Case D: $L_{op} = 9.53$ cm.

Fig. 5 Power spectral density of the pressure signal at point $\mathbf{P}_2$ in the experiment.

case A in Fig. 5(a), combustion is relatively stable and two small peaks emerge from the broadband noise. However, case B in Fig. 5(b), corresponding to the onset of the unstable zone (*cf.* Fig. 3(b)) exhibits multiple sharp harmonics. As seen from the spectrogram (Fig. 3(b)), higher harmonics appear nearly simultaneously, and the instability level grows by two orders of magnitude. For case C in Fig. 5(c) the instability is still very intense, conditions under which the fundamental mode is always dominant. Finally case D in Fig. 5(d) corresponds to the downfall of the instability so that only a couple of harmonics are still visible.

This section only gives a brief overview of the conditions encountered in the CVRC nevertheless, some interesting features typical of real-engine combustion instabilities were shown such as:

- Existence of an unstable range of L_{op} bounded by relatively stable operating conditions.

- Massively unstable operating points with highly non-linear pressure signal and rich harmonic content.

- Hysteresis was exhibited, depending on the translation direction of the oxidizer inlet.

These features are very hard to predict with numerical simulation tools and it is the challenge of the present paper to see if they can be recovered and how much *a priori* knowledge of the flame response is required for these predictions.

IV. Results of the numerical simulations

This section is organized in four subsections corresponding to each contributor. First the results obtained by Bertin Technologies and CNES using the solver CPS-C are presented in Sec. IV A. They have performed 2D axi-symmetric computations using a LES subgrid-scale model. Seven operating points are presented, exploring the whole range of the oxidizer-post length, thus providing a complete stability map. Then, the 3D LES of IMFT is described in Sec. IV B, for a single value of oxidizer-post length, L_{op}. The focus is set on the influence of the ignition procedure on the development of the instability. Variations in L_{op} are explored with a Helmholtz solver, using the flame response from the LES, in order to predict the stability map of the burner. The 3D LES of ONERA is presented in Sec. IV C, also for a single oxidizer-post length. Flame stabilization mechanisms are discussed as well as a detailed description of the unstable mode. The influence of the turbulent-combustion model is also studied. Finally in Sec. IV D, the contribution of Technische Universität München includes the use of a Linearized Euler Equation (LEE) solver to explore the stability map of the CVRC. The flame response model is extracted from a URANS computation by relating the unsteady heat release rate of the flame to the vorticity generation at the entrance of the combustion chamber.

A. Bertin Technologies and CNES

Numerical simulations have been performed with the CPS-C software, using a full Navier-Stokes approach, to assess the capability of the solver to predict the occurrence of longitudinal combustion instabilities. Validation is mainly based on the comparison between experimental and numerical results in terms of pressure oscillations and stability domain. The aim of these simulations is also

to better identify and to understand the mechanisms causing the combustion instability.

1. Numerical modelling

The CFD code used for the computational analysis is an in-house code called CPS-C (for Code de Propulsion Spatiale) developed by Bertin Technologies in collaboration with CNES. This code solves the Navier-Stokes equations in conjunction with the continuity, energy, turbulence and species equations. The numerical procedure is based on a second-order in space, approximate Riemann solver that allows the evaluation of spatial fluxes at cell faces whereas second-order accuracy in time is achieved by a two-step explicit scheme. The main physical models used in these computations are:

1. Perfect-gas law and temperature-dependent thermodynamic properties to represent the multi-species gaseous mixture,
2. The effects of turbulence are accounted for with a SGS-Mixt model [10],
3. The combustion process is represented by a 9-species mechanism with 17 finite-rate reactions, based on the Eklund kinetic scheme for H_2/O_2 and Dryer kinetic scheme for lean CH_4/O_2 combustion.

All the numerical simulations have been performed using a 2D axisymmetric approach, as a first step to assess the capability of CPS-C code to model longitudinal combustion instabilities in a rocket combustor.

The computational domain includes a simplified oxidizer injector (uniform subsonic inlet), the fuel collar, the entire chamber as well as the exit nozzle, which ensures that the outflow remains choked during the expected pressure oscillations. Several meshes, corresponding to different values of the oxidizer-post length (L_{op}), have been generated using isotropic and uniform cells size (about 0.5 mm). A zoom on the combustor entrance is shown in Fig. 6.

The values of L_{op} that have been computed are given in Tab. 3. The same parameters have been kept for all simulations, including the boundary conditions:

- Imposed stagnation temperature and mass flowrate at the inlet of the oxidizer post.

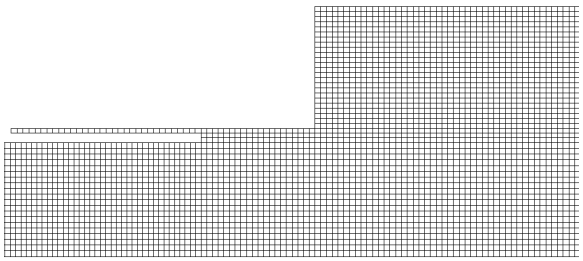

Fig. 6 Mesh - zoom on the combustion chamber entrance

Table 3 List of computations performed by Bertin Technologies with the CPS-C solver.

Case	1	2	3	4	5	6	7
L_{op} [cm]	9	11	12	13	14	15	19
Stability	S	U	U	U	U	U	S

- Imposed stagnation temperature and mass flowrate at the inlet of the fuel injector.
- Imposed static pressure (low value) at the nozzle exit until the nozzle is choked, then supersonic condition.

Numerical probes have also been defined in order to track pressure fluctuations at the same location as in the experiment (*cf.* Fig. 1).

2. Main results

The instantaneous flow-field in the chamber can be observed on temperature plots as shown in Fig. 7. Vortices are created from the shear layer between oxidizer, fuel streams and the tempera-

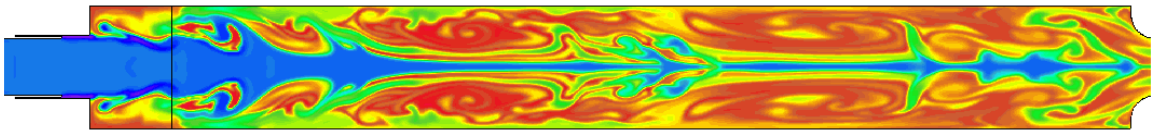

(a) $L_{op} = 14$ cm.

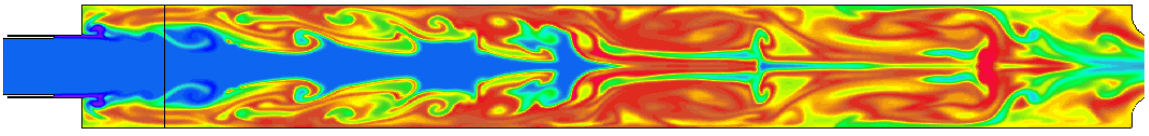

(b) $L_{op} = 19$ cm.

Fig. 7 Longitudinal cut of temperature fields for two values of the oxidizer-post length.

ture heterogeneities in the upstream part of the chamber. The plots correspond to instantaneous snapshots that show the highly turbulent nature of the flow in the combustion chamber as well as the large coherent structures involved in the instability.

The analysis is now complemented with the temporal evolution of the pressure at the probes. The peak-to-peak amplitudes at probe P_2 as well as the corresponding frequency as a function of L_{op} are reported in Tab. 4. Numerical regimes are classified into two categories depending on the peak-to-peak pressure amplitude. The regime is considered as unstable when peak-to-peak pressure amplitude is greater than 0.6 MPa.

Table 4 Results of the simulations with CPS-C and comparison with the experimental data.

Case	1	2	3	4	5	6	7
L_{op} [cm]	9	11	12	13	14	15	19
Δ P [MPa]	0.30	0.35	0.65	0.70	0.80	0.50	0.40
Frequency [Hz]	N/A	N/A	1460	1470	1470	1380	1370
Experiment [Hz]	N/A	1398	1379	1355	1331	1312	N/A

Figure 8 shows the evolution of the pressure signal near the chamber entrance for $L_{op} = 14$ cm. The peak-to-peak pressure amplitude is about 4 bar during the first steps of the numerical simulation (stable regime), before growing and reaching an amplitude of pressure oscillations equal to 8 bar (unstable regime). This behavior has also been observed experimentally, with a peak-to-peak pressure amplitude twice greater for unstable regimes compared to stable ones.

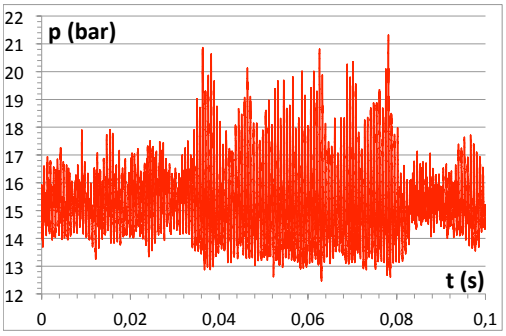

Fig. 8 Pressure signal - Lop = 14 cm

During the unstable regime, the amplitude of oscillations experimentally reaches 12 bar, whereas the peak-to-peak pressure amplitude does not exceed 8 bar numerically. This difference in amplitude, for the unstable regimes, can be due to the boundary conditions. Indeed, the combustion instabilities depend on the boundary conditions, and it has been shown that the amplitudes of oscillations are greater when the inlet of the oxidizer injector is supersonic (plug or slot inlet), compared to a uniform subsonic inlet [11]. It is recalled that the boundary conditions of the numerical model used in this contribution are slighlty different from the experimental geometry. The oxidizer injector is defined as a uniform subsonic inlet in the 2D numerical model whereas the experiment consists of a choked inlet (*cf.* Fig. 2(b)).

Unstable combustion is defined by the coupling between the pressure oscillations in the chamber and the heat-release fluctuations directly due to the combustion in the combustion chamber. Figures 9 and 10 present a comparison between the computed pressure evolution at probe P_2 (red curve) and the temporal variations of the volume averaged heat-release (normalized values on black curve), during the stable and unstable regime, respectively. For the unstable regime (Fig. 10), the cross-correlation between the two signals is 0.82, while it drops to 0.42 for the stable case (Fig. 9).

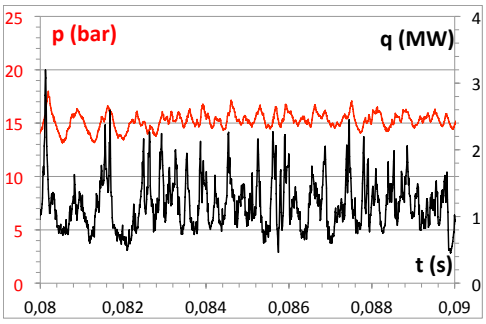

Fig. 9 Pressure and heat release - Stable regime

For the unstable regime at $L_{op} = 14$ cm, the frequency of pressure oscillations predicted by CPS-C is $F = 1470$ Hz, which is close to the experimental value of 1337 Hz. As for the other numerical simulations, this is due to the higher mean chamber pressure: 15 bar in the simulation versus 13.4 bar in the experiment. As explained in [12], this overestimation of the pressure could be due to an overestimation of the combustion efficiency or the lack of heat-losses in the simulation.

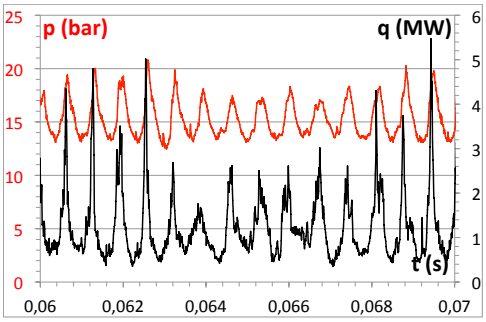

Fig. 10 Pressure and heat release - Unstable regime

These points are outside the scope of the present paper.

Numerical simulations of the CVRC experiment demonstrate the robustness of the solver CPS-C and its ability to describe combustion instabilities in a combustion chamber on 2D meshes with a reasonable computational cost. A good agreement has been obtained between the numerical and experimental results, in terms of both pressure oscillations and unstable regime range. A

	Lop inf [cm]	Lop max [cm]
CPS	$11 < Lop < 12$	$14 < Lop < 15$
EXP	12.07	16.76

Table 5 unstable regime range - Experimental and numerical results

cross-correlation level of 0.82, between peaks of pressure and heat release signals has been observed in the numerical computations during the unstable regime. The coupling leads to an increase of the pressure oscillations in the chamber with a peak-to-peak pressure amplitude twice greater for the unstable regimes compared to the stable ones.

B. IMFT

The objective of IMFT is to use two sets of tools to study different characteristics of the instabilities encountered in the CVRC.

1. **Large-Eddy Simulation** (LES): The AVBP solver (`www.cerfacs.fr/4-26334-The-AVBP-code.php`) is used to compute an unstable operating point at a fixed oxidizer-post length, $L_{op} = 4.75$ in (~ 12 cm). Because the analysis of the flame structure and the description of the instability have already been discussed elsewhere [12], the present contribution focuses on the influence of the ignition procedure.

2. **Low-Mach-number acoustics**: For parametric variations at low computational cost, it has been shown that acoustics solvers nicely complement LES or experimental data for the study of combustion instabilities [13]. Therefore, the influence of L_{op} will be assessed with the Helmholtz solver AVSP [14].

1. Large-Eddy Simulation of the ignition at fixed oxidizer-post length

The AVBP code solves the compressible Navier-Stokes equations on unstructured grids [15–17]. For this study, the second-order Lax-Wendroff scheme [18] was used together with the Smagorinsky LES model [19] and the Dynamically Thickened Flame (DTF) model [20] for turbulent combustion. The reaction of methane and oxygen is modeled with a two-step mechanism validated under the conditions of the CVRC [12]. The computational domains starts downstream of the choked sections for both fuel and oxidizer lines and it was checked that the imposed mass-flux boundary condition has an acoustic impedance consistent with the theoretical value, $Z = -1/M_{ox}$, where M_{ox} is the mean Mach number in the oxidizer post. The exit nozzle is fully meshed, allowing a well-defined set of boundary conditions. The reader is referred to [12] for a thorough description of the computational setup.

For studies devoted to the steady-state behavior of a combustor, it is often impractical – sometimes impossible– to replicate the ignition procedure of the experiment in a simulation. Usually, this is because of the duration of the ignition sequence or the time necessary to reach a steady-state. The complexity of the physical mechanisms involved at ignition can also be a major hurdle and their modeling is an issue *per se*. In the case of the CVRC, both problems arise, with a sequence taking about 5.5 s and involving dual-fuel injection and auto-ignition of JP-8. Consequently, alternate ignition procedures are devised for the LES.

Like in the experiment, the LES starts with a non-reacting flow: at $t = 0$, the chamber is filled with oxidizer at rest, pressurized at 13.4 bar, which is the experimental operating pressure for Case A, and both oxidizer, $\dot{m}_{ox}$, and fuel, $\dot{m}_f$, mass flow rates are imposed at their respective inlets. The simulation is advanced to $t = 4$ ms for the velocity field to develop and it is ignited (*cf.* Fig. 11) using one of the following procedures:

1. **IGNIT-X** (Fig. 11(a)): The whole chamber ($x > 0$) is filled with burnt gases, with a linear transition over 1 cm. Only the composition and temperature are altered, the velocity and pressure fields are kept from the non-reacting simulation.

2. **IGNIT-Z** (Fig. 11(b)): The mixture-fraction field, z, is computed and the regions where $0.08 < z < 0.11$ are filled with burnt gases.

(a) IGNIT-X.

(b) IGNIT-Z.

Fig. 11 Longitudinal cut of temperature fields for both ignition procedures.

Figure 12(a) shows the evolution of the mean pressure in the computational domain. For $t < 4$ ms, it decreases to 10.4 bar because the initial pressure is not consistent with this non-reacting flow. Once the flow has been ignited, the two procedures yield drastically different evolutions. **IGNIT-X** shows a monotonous increase of the pressure over 10 to 12 ms until the permanent regime has been reached. This can be described as a smooth ignition. However, **IGNIT-Z** exhibits a pressure spike, reaching 21 bar in less than 1 ms followed by a decrease to the same mean pressure as **IGNIT-X**. This kind of event is often referred to as *hard ignition*. Moreover, periodic pressure fluctuations corresponding to a combustion instability are observed after **IGNIT-Z**. The concomitant evolution of the heat-release rate is presented in Fig. 12(b). The chemical source term is disabled during the cold flow, therefore, there is not signal for $t < 4$ ms. For both cases, the combustion converges much faster than the pressure and consistently with Fig. 12(a), there is a

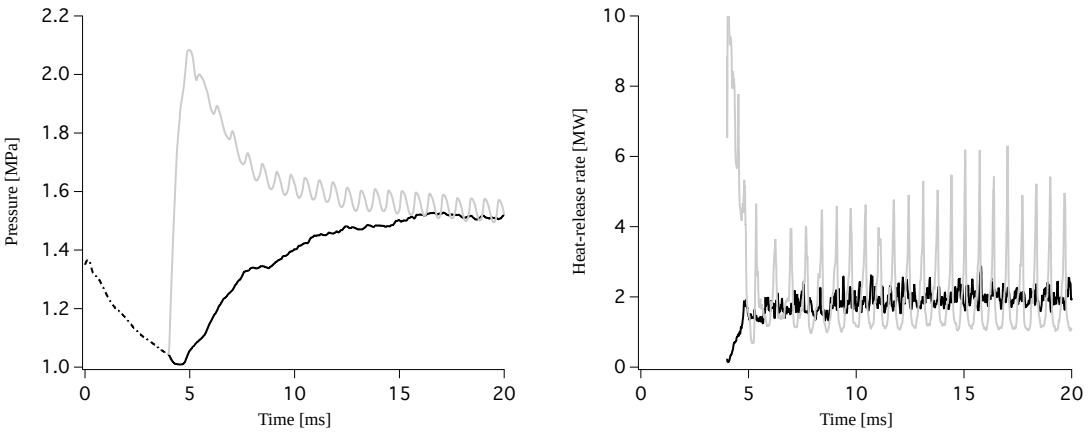

(a) Mean pressure.

(b) Pressure at probe P_2.

Fig. 12 Temporal evolution of pressure and heat-release rate during the ignition sequence. Cold flow: -·-·- ; IGNIT-X: —— ; IGNIT-Z: —— .

burst of heat-release rate for **IGNIT-Z**, while **IGNIT-X** is more stable. Turbulent fluctuations are observed for **IGNIT-X**, but a strong combustion instability is triggered by the hard ignition **IGNIT-Z**, which does not seem to develop with the smooth ignition.

The analysis of Fig. 12 suggests that the CVRC is linearly stable for this value of L_{op} but an instability can develop if the flow field is shaken. This mechanism called triggering has already been described and modeled in simpler configurations [21]. The instability can be recovered in **IGNIT-X** by adding a half-wave mode pressure perturbation in the combustion chamber (not shown), which demonstrates that the linearly-stable regime reached after **IGNIT-X** can be destabilized with a finite-amplitude acoustic perturbation.

2. Low-Mach-number acoustics at variable oxidizer-post length

An alternative to brute-force LES for the numerical simulation of combustion instabilities is to solve only for acoustics, accounting for unsteady combustion through a source term. This technique requires much less CPU time and provides the list of acoustic eigen-modes: frequency and amplification rate. It will now be used to assess the influence of the oxidizer-post length on the stability of the CVRC. For the present contribution, linear acoustics at small Mach number are considered,

resulting in a modified Helmholtz equation:

$$\nabla \cdot \left(\frac{1}{\rho_0} \nabla p' \right) - \frac{1}{\gamma p_0} \frac{\partial^2 p'}{\partial t^2} = - \frac{\gamma - 1}{\gamma p_0} \frac{\partial q'}{\partial t} \tag{1}$$

where p' is the pressure fluctuation, q' the heat-release rate fluctuation, ρ_0 the baseline density, p_0 the baseline pressure and γ the ration of heat capacities. The Helmholtz solver AVSP [14] was used, which solves Eq. 1 in the frequency domain on unstructured grids. The computational domain starts downstream of the choked inlets and stops before the exit nozzle. Indeed, Mach-number effects can not be neglected in these regions and have to be modeled through appropriate boundary impedances. The mesh requirements are much less stringent than for the LES so that only 200 000 cells are necessary.

The unsteady heat-release rate, q', is modeled with a local Flame Transfer Function [22], which is an extension of the $n-\tau$ model [23, 24]. The parameters of the FTF are evaluated on the unstable LES and are assumed to be independent of the frequency. This is arguably a rough approximation, which is driven by pragmatism (we do not have simulations at other frequencies) but also justified by the modest variation of the frequency of the unstable mode when L_{op} is varied ($\sim \pm 16\%$).

Last but not least, the specification of the boundary conditions is central for the computation of the eigen-modes. The particularity of this configuration is that the acoustic solver uses the zero-Mach-number approximation, which is not valid in the inlet and outlet sections. Describing strategies that account for non-zero Mach number boundary effects in a Helmholtz solver is beyond the scope of this paper but various values of the impedance, Z, were tested with the intent to reproduce the stability map of the experiment when L_{op} is varied. The first thing to do is to chose a set of variables for the definition of the impedance. Classically, Helmholtz solvers use pressure and velocity fluctuations, (p', u'), while Linearized Euler Equation (LEE) solvers that account for convective effects tend to use total enthalpy and mass flow rate fluctuations, $(J', \dot{m}')$. This choice is guided by the definition of a proper acoustic energy. Both sets of variables are equivalent and use a consistent definition of the impedance:

$$Z_{p,u} = \frac{p'}{\rho_0 \; c_0 \; u'} \tag{2}$$

$$Z_{J,m} = \frac{\rho_0 \; J'}{c_0 \; \dot{m}'} \tag{3}$$

where c_0 is the baseline speed of sound. One can easily show that:

$$Z_{J,m} = \frac{Z_{p,u} + M}{M\ Z_{p,u} + 1} \tag{4}$$

where M is the Mach number. Three choices for the boundary conditions Z^{in} and Z^{out} are considered in this work:

1. **Case 1: The value of $Z_{p,u}$ is used**. The inlet is supposed to have a constant mass flux (*i.e.* $\dot{m}' = 0$), which yields $Z^{in} = Z_{p,u} = -1/M_{ox}$. The outlet impedance is calculated from the compact approximation of Marble and Candel [25], that is $Z^{out} = Z_{p,u} = -2/((\gamma - 1)M_{ch})$. With $M_{ox} = 0.32$, $M_{ch} = 0.18$ and $\gamma = 1.18$, this yields $Z^{in} = -3.13$ and $Z^{out} = -61.7$.

2. **Case 2: The value of $Z_{J,m}$ is used**. The values of $Z_{p,u}$ are fed into Eq. 4, which yields $Z^{in} = \infty$ and $Z^{out} = -5.11$

3. **Case 3: The impedances are tuned** to allow a better representation of the experimental stability map: $Z^{in} = Z^{out} = -10$.

The other boundaries are treated as rigid walls, imposing no velocity fluctuation *i.e.* $u' = 0$.

The results are presented in Fig. 13 where the baseline conditions (fields of pressure and speed of sound) are taken from the LES of Sec. IV B 1. A negative value of the damping indicates a stable

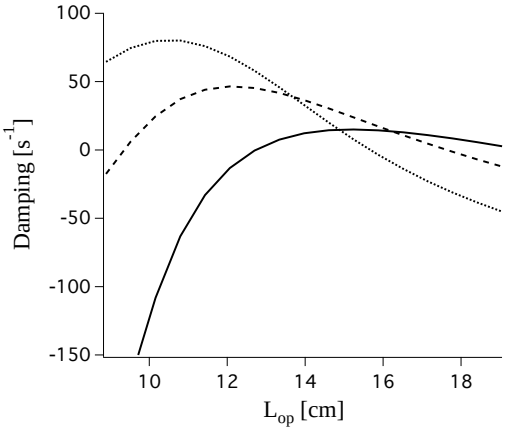

Fig. 13 Damping rate of the second acoustic mode versus L_{op}, computed with AVSP. Case 1: ——— ; Case 2: ····· ; Case 3: - - - - .

mode while positive values correspond to linearly unstable conditions. In fact, because losses are

not accounted for in the Helmholtz solver, the damping has to be above a certain positive value so that the energy from the flame overcomes the losses. A precise evaluation of the losses is an issue *per se* and was not done here. All cases present both a stable and an unstable range. For Case 1, acoustic losses through the boundaries are overestimated resulting in a very small unstable range. On the other hand, Case 2 overestimates the unstable range at small L_{op}. Tuning the impedances in between the two extreme cases gives a qualitatively correct representation of the unstable range for this configuration. Obviously, these results are qualitative but the methodology is generic and shows great potential.

C. ONERA

The objective of ONERA is to perform a Large-Eddy Simulation of an unstable operating point with the CEDRE solver (`http://www.aerospacelab-journal.org/CEDRE-Software`). In order to have the opportunity to compare this computation with both the experiment and other simulations, it was decided to present here the same operating point as in [12], which corresponds to a Case A (Tab. 1) and a fixed oxidizer-post length, $L_{op} = 4.75$ in (~ 12 cm). For a fair comparison, modeling and numerical parameters were kept as close as possible to those of [12]:

1. The computational mesh is the same and was provided by R. Garby.

2. Turbulent combustion is modeled by the Dynamically Thickened Flame (DTF) model [20].

3. The LES model is that of Smagorinski [19].

Nevertheless, some differences remain, essentially in the numerics: CEDRE uses a cell-centered finite-volume HLLC scheme for the Euler fluxes with a first-order implicit time advancement and a second-order in space, while the AVBP solver used in [12] employs an explicit cell-vertex formulation, second order in space and time. There may also be further differences hidden in the details of the implementation, which could impact the solution but are very difficult to uncover. As straightforward as it may seem, comparing different solvers on the same operating point is a very stringent test [26]. This exercise typically falls within the Uncertainty Quantification paradigm: an attempt to evaluate the error bars associated to numerical simulations.

1. Flame stabilization

A prerequisite for the study of combustion instabilities is the accurate prediction of flame stabilization mechanisms. Figure 14 presents a longitudinal cut of the heat-release rate field with two

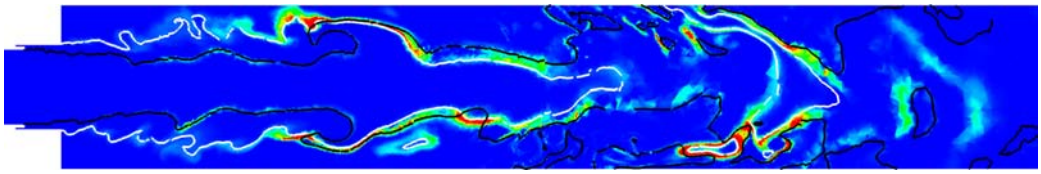

Fig. 14 Longitudinal cut of heat-release rate field with stoichiometric (black) and $T = 2000$ K (white) iso-contours.

iso-contours superimposed: stoichiometric mixture fraction (in black) and $T = 2000$ K (in white). The first characteristic of this flame is that it is not attached, as seen by the lack of heat release rate close to the lip of the injector. For this particular snapshot, it stands as far as one oxidizer-post diameter away from the inlet of the chamber and even further from the methane injection. Three different combustion regions may be seen: (1) a weak diffusion branch sitting on the stoichiometric line, (2) a weak reaction zone on the $T = 2000$ K iso-contour and (3) further downstream, an intense reaction zone where the two iso-contours meet. This peculiar flame structure is similar to that observed in [12] and is referred to as a 'burnt-gas stabilized flame'. Indeed, it turns out that the recirculation of hot gases at the entrance in the combustion chamber is instrumental for the stabilization of this flame, which may not be typical of operational rocket engines. Finally, when comparing Fig. 14 and Fig. 6 in [12] it seems that the flame is longer for the present computation, with small reacting pockets flowing through the exit nozzle.

2. Analysis of the instability

This LES performed with CEDRE presents a self-sustained combustion instability, as evidenced by the pressure signal recorded at point P_2, presented in Fig. 15(a). The peak-to-peak pressure fluctuations reach as much as 0.15 MPa, which is significant but almost one order of magnitude smaller than in the experiment (*cf.* Fig. 3(a)). The spectrum of this signal is presented in Fig. 15(b) and shows a strong peak at a frequency $F = 1596$ Hz (with a spectral resolution of 120 Hz). This frequency is higher than the experimental value, $F^{xp} = 1392$ Hz (*cf.* Tab. 2), but this is

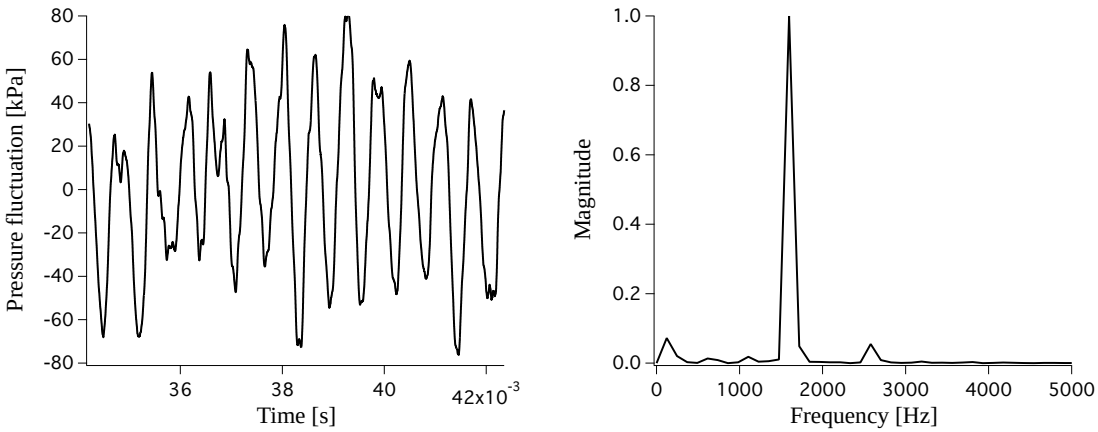

(a) Pressure fluctuation at probe P_2.

(b) Pressure spectra at probe P_2.

Fig. 15 Pressure signal and spectra recorded at probe P_2.

fully consistent with the fact that the LES predict larger mean pressure, resulting in a higher average sound speed. This overestimation of the unstable frequency is common to many LES of this configuration [12, 27] and could be related to the underestimation of heat losses.

Thanks to the implicit temporal integration available in CEDRE, the numerics remain stable even for large values of the acoustic CFL number, λ. However, it was observed that as the time step is increased, the dissipation terms in the numerics greatly impacted the amplitude of the instability. The present results were obtained with a time step $\Delta t = 10^{-7}$ s, which corresponds to a maximum CLF number $\lambda = 2$ for the smallest cells. Increasing λ by a factor 10 yields a decrease of the amplitude of the instability by a factor 3. It was also checked that a further decrease of the time step did not increase the magnitude of the pressure fluctuations.

3. Influence of model parameters on the unstable mode

With the intent to further investigate the uncertainties inherent to numerical simulations, the influence of the turbulent-combustion model parameters is tested. The DTF model [20] applies local thickening to the flame front so as to be resolved on the LES mesh. The thickening function is driven by one numerical parameter: the number of points in the flame thickness, N_δ. Then an efficiency function is used to recover the lack of flame surface due to the alteration of the flame / turbulence interaction by the thickening [28]. The efficiency function has four parameters: the laminar flame speed, s_L^0, and thickness, δ_L^0, a global parameter, β and a characteristic length of the turbulent

structures, L_T. The original parameters were obtained by the simulation of a stoichiometric laminar flame under the conditions of Case A. The parameters have then been altered in order to mimic a

Table 6 Parameters for the DTF model.

	s_L^0 [m/s]	δ_L^0 [μm]	β	L_T [m]	N_δ
Original	1.52	35.4	0.7	$1.0\ 10^{-2}$	5
Modified	0.436	195	3	$2.2\ 10^{-2}$	8

much slower laminar flame: the premixed flame at the global equivalence ratio of the experiment. All the parameters for this so-called *modified* simulation as well as the *original* one are recalled in Tab. 6. The values of β, L_T and N_δ also had to be altered for the *modified* simulation in order to stabilize the flame. Consequently, the proposed modification of the DTF model parameters resulted

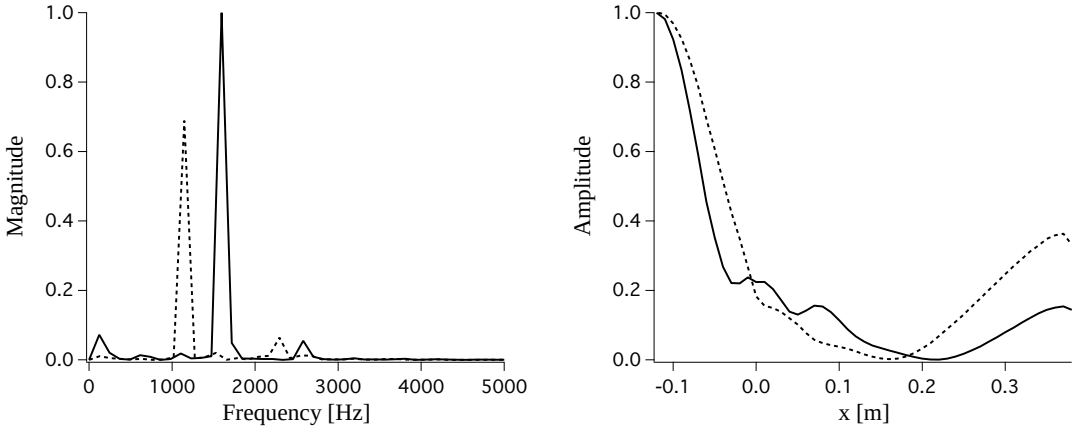

(a) Pressure spectra at probe P_2.

(b) Longitudinal mode shape.

Fig. 16 Influence of turbulent combustion model parameters on the unstable mode. —— : original; - - - - : modified.

in a similar flame stabilization (not shown) as well as a self-sustained instability except that the unstable mode was different. The spectra of the pressure at probe P_2 presented in Fig. 16(a), shows that the unstable frequency has been shifted down to $F_m = 1146$ Hz and its amplitude has also been reduced. The longitudinal structure of the pressure fluctuations is shown in Fig. 16(b): both modes seem to share very similar shapes with a pressure node inside the combustion chamber and an anti-node at the boundaries.

The use of a Helmholtz solver to compute the acoustic modes of the configuration can shed

light on this frequency change. For this purpose, the solver AVSP was used [14] and more details are given in Sec. IV B 2 about the modeling of the CVRC. The Helmholtz solver predicts that the first two longitudinal modes have frequencies of $F_1^H = 1226$ Hz and $F_2^H = 1657$ Hz, which are fairly close to the ones measured in the *modified* and *original* CEDRE computations. It then seems plausible that the response of the LES to the DTF model parameter variation corresponds to a switch from the second to the first acoustic mode. For qualitative validation, the shape of these modes computed with the Helmholtz solver are plotted in Fig. 17 and compare favorably with the LES result of Fig. 16(b).

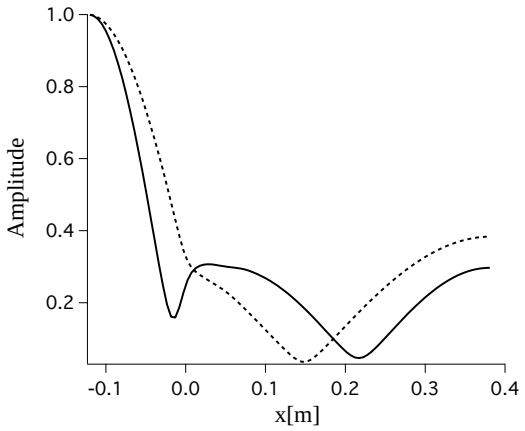

Fig. 17 Modulus of the first two acoustic modes computed with the Helmholtz solver AVSP. ---- : first mode ($F_1^H = 1226$ Hz); —— : second mode ($F_2^H = 1657$ Hz).

Interestingly, a similar mode-switching behavior has been observed in the experiment, though for a different oxidizer-post length ($L_{op} = 17.15$ cm). In the experiment, a mild instability at 1210 Hz transitions to a strong instability at 1290 Hz. This frequency change is more modest than in the present LES but this is likely due to the different oxidizer-post length resulting in companion acoustic modes to be much closer as the two tubes are almost in tune.

D. Technische Universität München

For this contribution, a hybrid approach is presented, which uses a standard CFD tool to simulate combustion and fluid-dynamics and a code based on the Linearized Euler Equations (LEE) that solves for acoustic waves. CFD provides the steady state reacting flow field and parameters

for the flame response in the acoustic solver. A so-called *vorticity feedback* model, based on the n-τ model of Crocco, couples acoustics and unsteady heat release rate through the unsteady generation of vorticity at the lip of the burner. Both parameters n and τ are obtained from CFD.

1. Methodology

An unsteady 2D axisymmetric RANS computation is performed for a fixed value of $L_{op} =$ 19.05 cm in order to evaluate the flame-response parameters. The outlet nozzle is not taken into account. Instead, a harmonic excitation with a frequency of 1400 Hz is applied at the location of the nozzle entrance to force a longitudinal mode in the chamber. Following on the idea that large coherent vortical structures [7, 29, 30] may be responsible for flame wrinkling and the subsequent generation of unsteady heat release rate, the current *vorticity feedback* model relates the flame response to the generation of vortices. As for the model of Crocco [3], two parameters denoted n and τ are defined by

$$\dot{q}'(t) = n \cdot \Omega'(t - \tau), \tag{5}$$

where $\dot{q}'$ is the heat-release rate fluctuation and Ω' the vorticity integrated in a control volume. n corresponds to an amplification factor while τ is the time delay between vortex generation and combustion response. For consistency, the measurement of Ω' in the URANS and LEE simulations

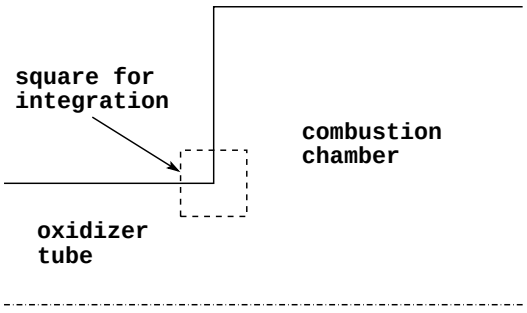

Fig. 18 Representation of the control volume for the integration of the vorticity signal Ω'.

must be identical. However, linearized equations correctly describe the evolution of vorticity only for small amplitudes. As the magnitude of vorticity disturbances grow, dissipation and dispersion come into play. Because these effects are not included in the LEE, the control volume to determine

Ω' is chosen as a small region at the cross-section change, where vorticity is generated and remains in the linear regime (*cf.* Fig. 18).

The numerical values for n and τ evaluated in the URANS computation are given in Tab. 7. Normalized values are also presented, which are defined as

$$n^* = \frac{n}{c_0^2 L_0 \rho_0} \tag{6}$$

$$\tau^* = \tau \frac{c_0}{L_0} \tag{7}$$

$$\Omega'^* = \frac{\Omega'}{c_0 L_0} \tag{8}$$

$$\dot{q}'^* = \frac{\dot{q}'}{c_0^3 L_0^2 \rho_0} \tag{9}$$

with $L_0 = 1$ m, $c_0 = 675$ m/s and $\rho_0 = 3.55$ kg/m^3. The unsteady heat release rate from Eq. 5 is im-

	$\lvert\dot{q}'\rvert$	$\lvert\Omega'\rvert$	n	τ
dimensional	1223 W	$9.46\ 10^{-4}$ s^{-1}	$1,292,811$ J	$3\ 10^{-4}$ s
normalized	$1.12\ 10^{-6}$	$1.40\ 10^{-6}$	0.8	0.2025

Table 7 Dimensional and normalized parameters n and τ for the *vorticity feedback* model.

posed as a source term in the energy equation in the LEE solver. The flame location computed from the steady state RANS simulation defines the region where this term is applied. The computational domain starts immediately downstream of the choked inlet and ends after the exit nozzle. Also, the small slit for methane injection is not meshed in the LEE because of the resulting constraint on the time step and its lack of influence on the acoustic modes of the configuration. Finally, because the LEE simulations are performed on a 3D domain, only the azimuthal component of Ω' is considered.

2. Results

Even though, in the experiment, L_{op} is varied continuously, the numerical study assumes a quasi-steady state of the instability and considers only the four fixed positions given in Tab. 2. For these positions the resonant frequencies are evaluated and the wave-form along the longitudinal axis is presented. The LEE calculations also provide the growth rates for these positions. However, this approach does not give any information about the limit cycle because the *vorticity feedback* model (*cf.* Eq. 5) is only valid in the linear regime. Moreover, this procedure assumes that the values

of n and τ provided by a single URANS computation are independent of L_{op}. This assumption is deemed reasonable because the generation of vortices is unlikely to be affected by the oxidizer-tube length and also because the variation in unstable frequency versus L_{op} is modest.

Because the LEE equations are solved in the time domain, the stability is determined by performing a Fourier Transform of the impulse response of the system. A Gaussian perturbation, exciting a broad range of frequencies is used as the initial condition and the pressure at probe P_2 is recorded for the analysis (*cf.* Fig. 1).

The results for the four values of L_{op} are presented in Fig. 19, which includes two series of computations. First, the response without the *vorticity feedback* model (grey lines) and then with the model activated (dark lines). These results are normalized by the peak amplitude so as to be compared on a single scale. Without unsteady combustion, the peaks in the pressure signal Fourier Transform correspond to the eigenfrequencies of the configuration. When the unsteady heat release rate is accounted for, only one of these modes is selected, except for $L_{op} = 9.53$ cm (*cf.* Fig. 19(d)). Indeed, this configuration is predicted as stable by the present LEE, while the others are unstable. For all the unstable cases, the second longitudinal acoustic mode is amplified with combustion.

The list of the dominant frequencies with combustion are presented in Tab. 8. The agreement

	Frequency [Hz]		
L_{op} [cm]	LEE	Experiment	Relative difference
19.05	1125	1215	−7.4 %
16.76	1191	1282	−7.1 %
11.43	1237	1392	−11.1 %
9.53	1230	1379	−10.8 %

Table 8 Comparison of resonant frequencies for different values of L_{op}.

is good for $L_{op} = 19.05$ cm however, as the oxidizer post is shortened, the discrepancy between LEE and experiments increases. Nevertheless, the overall trend is correct, in particular the similar values between the two shorter L_{op}, which is also observed in the experiment.

Then the pressure traces are used to evaluate the growth rate of the instability. All the cases show an exponential increase of the pressure fluctuations, except for the shortest post length. Indeed,

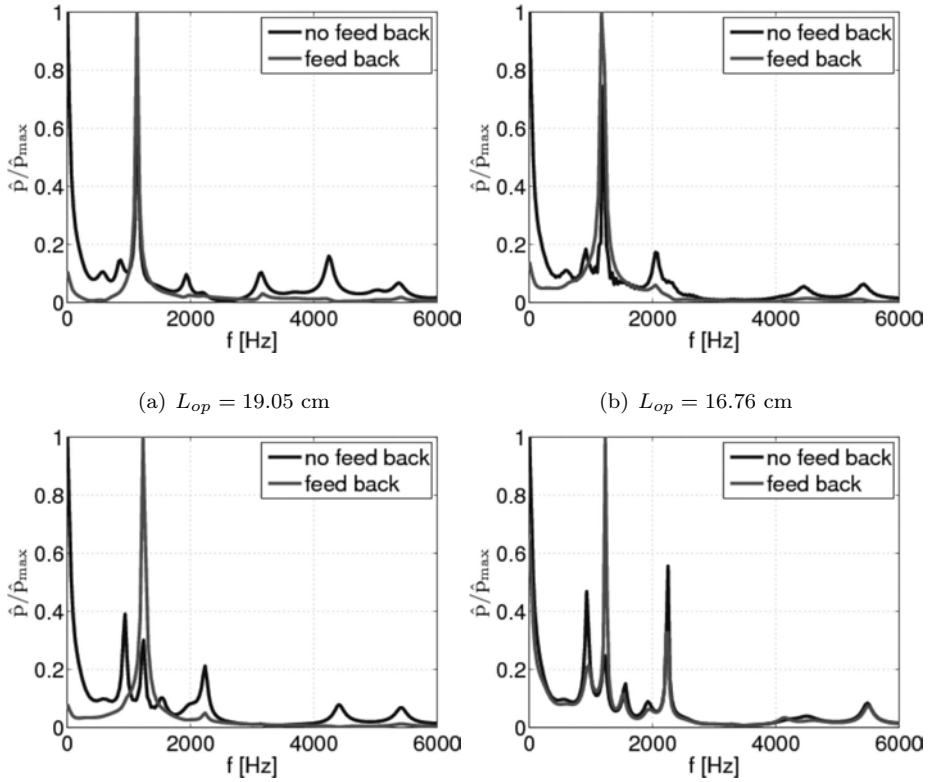

(a) $L_{op} = 19.05$ cm (b) $L_{op} = 16.76$ cm

(c) $L_{op} = 11.43$ cm (d) $L_{op} = 9.53$ cm

Fig. 19 Spectra of the impulse response for four values of L_{op}, measured at probe P_2 with the LEE solver.

for $L_{op} = 9.53$ cm the initial pressure perturbation decays, which is consistent with the spectra of Fig. 19(d). For the unstable cases, the growth rates are determined by applying an exponential fit

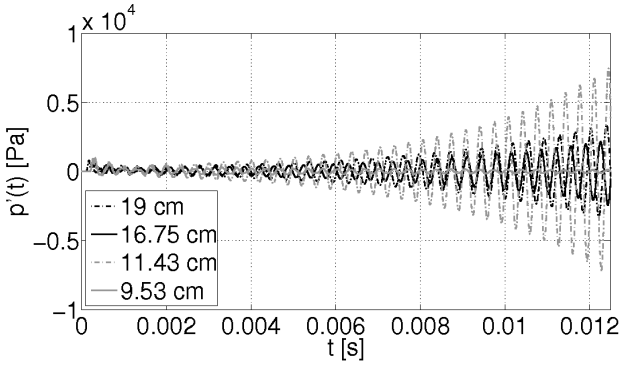

Fig. 20 Pressure time traces at probe P_2 for different values of L_{op}.

to the evolution of the amplitude of the pressure signal versus time and the results are reported in Tab. 9. The estimation from the LEE underestimates the experimental values, however, the trend

	Growth rate [s^{-1}]	
L_{op} [cm]	LEE	Experiment
19.05	87	134
16.76	88.5	199
11.43	109.6	344
9.53	N/A	180

Table 9 Comparison of damping rates versus L_{op}.

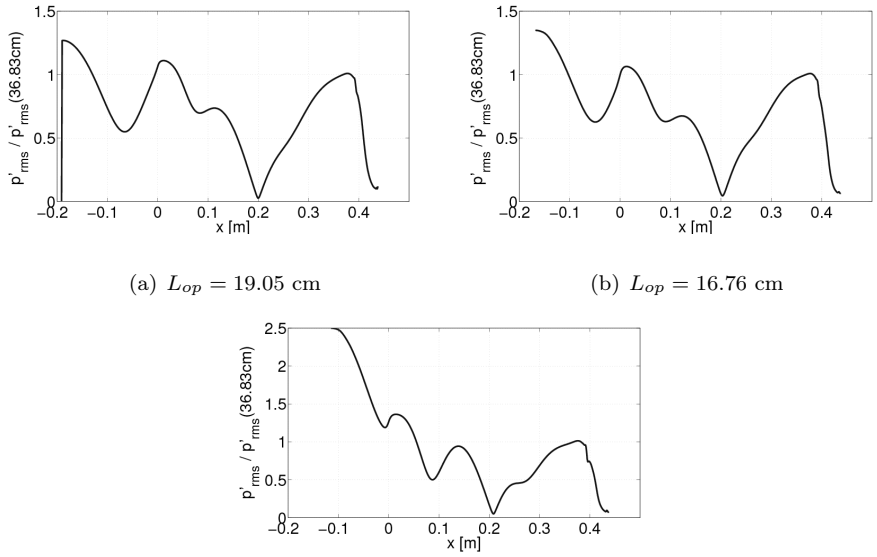

(a) $L_{op} = 19.05$ cm

(b) $L_{op} = 16.76$ cm

(c) $L_{op} = 11.43$ cm

Fig. 21 RMS value of the pressure over axial axis.

is recovered: the growth rate increases when L_{op} is decreased, except for the smaller value, which is stable in the LEE while showing a decrease in the experiment.

Finally, the mode shapes for the unstable cases are reported in Fig. 21. The root-mean-square pressure fluctuation is plotted versus the longitudinal coordinate, x, and normalized by its value at 36.83 cm downstream of the fuel injector. The mode shapes are very similar for $L_{op} = 19.05$ cm (Fig. 21(a)) and $L_{op} = 16.76$ cm (Fig. 21(b)), with comparable amplitudes in the chamber and the injector. However, for $L_{op} = 11.43$ cm (Fig. 21(c)) the amplitude of the pressure fluctuation is much larger in the oxidizer tube than in the chamber.

V. Conclusion

This compilation of research efforts, towards the prediction of the occurrence of combustion instabilities in a model rocket combustor has shown how numerical simulations can reproduce many features of stable and unstable operating conditions. Two types of numerical simulations have been presented: (1) Large-Eddy Simulations for a very detailed reproduction of the unsteady flame and flow dynamics and (2) Helmholtz or LEE solvers that only solve for acoustics while requiring additional input to mimic the presence of the flame.

Three LES have been presented. First the group of Bertin Technologies and CNES have shown that the CSP-C solver can perform unsteady 2D-axisymmetric simulations at a reasonable CPU cost. They have explored the whole range oxidizer-post length, resulting in a stability map in good agreement with the experiment. They could qualitatively discriminate between stable and unstable conditions. Then IMFT and ONERA both presented a 3D LES of the same operating point with the solver AVBP and CEDRE, respectively. These simulations showed consistent flame stabilization and instability mechanisms. Moreover, very interesting features were described, such as mode switching and hysteresis between stable and unstable for a fixed operating point. Such behavior can only be tackled with 3D LES and are very promising points for the future developments in numerical simulations of unstable engines.

Two groups have used acoustic solvers to explore the stability map. While IMFT have used a Helmholtz solver (AVSP), which assumes zero Mach number, TUM have used a LEE solver (PIANO) that accounts for mean flow effects. An other difference is that while AVSP finds the eigenmodes in the frequency domain, PIANO solves for acoustics in the time domain. Both were fitted with a rather simple model for the flame response, only valid for one frequency. Nevertheless, the two approaches were able to predict an unstable range as well as an important qualitative feature of the CVRC that is a maximum growth rate of the instability for intermediate values of L_{op}.

Overall, this paper covers the most advanced simulation techniques for the prediction of combustion instabilities, each of them being a different compromise between computational cost, accuracy and need for *a priori* knowledge of the flame response. This study, like most current work on combustion instabilities, shows that the numerical tools have a great potential but significant sources

of uncertainties remain for the simulations to become quantitative. Obviously, modeling the flame response is a central matter but the determination of acoustic boundary conditions as well as the precise evaluation of acoustic and heat losses are also crucial.

Acknowledgments

IMFT and ONERA were granted access to the high-performance computing resources of CINES under the allocation c2011_026625 made by Grand Equipement National de Calcul Intensif.

Bertin Technologie and CNES acknowledge the financial support of 'CNES Launchers Directorate R&D program'.

Technische Universität München would like to acknowledge the financial support of the German Research Council (DFG) in the framework of the Sonderforschungsbereich Transregio 40 and The Leipniz - Rechenzentrum for offering access to computational resources. Additional thanks go to the DLR Braunschweig for granting us access to the acoustic solver PIANO.

The authors would like to acknowledge the valuable input of additional people who were involved in this research work: Romain Garby from IMFT, Aurélie Nicole and Gérard Ordonneau from ONERA, Professor Thomas Sattelmayer and Daniel Morgenweck from TUM, and Yen Ching Yu, Stan Rosen, Ajay Madhav, Akash Patel and Michael Bedard from Purdue University.

References

[1] JWS Rayleigh Lord. The explanation or certain acoustic phenomena. *Nature*, 18:319, 1878.

[2] W. R. Hawthorne. Theory of Combustion Instability in Liquid Propellant Rocket Motors, by Luigi Crocco and Sin-I Cheng. London: Butterworths Scientific Publications; New York: Interscience Publishers Inc.; 1956. 200 pp. *J. Fluid Mech.* , 2(1):100–104, March 1957.

[3] Luigi Crocco and Sin-I Cheng. *Theory of combustion instability in liquid propellant rocket motors.* Butterworths Scientific Publications, London, agardograp edition, 1956.

[4] FEC Culick. *Unsteady motions in combustion chambers for propulsion systems.* NATO/RTO-AG-AVT-039, agardograp edition, 2006.

[5] Thierry Poinsot and Denis Veynante. *Theoretical And Numerical Combustion.* www.cerfacs.fr/elearning, third edition, 2011.

[6] Tim C Lieuwen. *Unsteady Combustor Physics.* Cambridge University Press, 2012.

[7] Y.C. Yu, L.A. O'Hara, J.C. Sisco, and W.E. Anderson. Experimental Study of High-Frequency Combustion Instability in a Continuously Variable Resonance Combustor (CVRC). In *47th AIAA Aerospace Sciences Meeting Including The New Horizons Forum and Aerospace Exposition*, number January, Orlando, Florida, 2009.

[8] J.C. Sisco, Y.C. Yu, V. Sankaran, and W.E. Anderson. Examination of mode shapes in an unstable model combustor. *Journal of Sound and Vibration*, 330(1):61–74, January 2011.

[9] Yen C. Yu, James C. Sisco, Stanford Rosen, Ajay Madhav, and William E. Anderson. Spontaneous Longitudinal Combustion Instability in a Continuously Variable Resonance Combustor. *J. Prop. Power* , 28(5):876–887, September 2012.

[10] Laure Coquart. *Large Eddy Simulation of the Unsteady Turbulent Transonic Flow through a 3D Nozzle.* PhD thesis, Université de Paris 06, Paris, France, 2001.

[11] Guoping Xia, Randy Smith, William Anderson, and Charles Merkle. Computational Simulations of the Effect of Chamber Diameter on Single-Element Rocket Combustor Instability. In *44th AIAA/ASME/SAE/ASEE Joint Propulsion Conference and Exhibit*, Reston, Virigina, July 2008. American Institute of Aeronautics and Astronautics.

[12] Romain Garby, Laurent Selle, and Thierry Poinsot. Large-Eddy Simulation of combustion instabilities in a variable-length combustor. *Comptes Rendus Mécanique*, 341(1-2):220–229, January 2013.

[13] L Selle, L Benoit, T Poinsot, F Nicoud, and W Krebs. Joint use of compressible large-eddy simulation and Helmholtz solvers for the analysis of rotating modes in an industrial swirled burner. *Combustion and Flame*, 145(1-2):194–205, April 2006.

[14] Franck Nicoud, Laurent Benoit, Claude Sensiau, and Thierry Poinsot. Acoustic Modes in Combustors with Complex Impedances and Multidimensional Active Flames. *AIAA Journal*, 45(2):426–441, February 2007.

[15] L Selle, G Lartigue, T Poinsot, R Koch, K-U Schildmacher, W Krebs, B Prade, P Kaufmann, and D Veynante. Compressible large eddy simulation of turbulent combustion in complex geometry on unstructured meshes. *Combustion and Flame*, 137(4):489–505, June 2004.

[16] V Moureau, G Lartigue, Y Sommerer, C Angelberger, O Colin, and T Poinsot. Numerical methods for unsteady compressible multi-component reacting flows on fixed and moving grids. *Journal of Computational Physics*, 202(2):710–736, January 2005.

[17] L.Y.M. Gicquel, G. Staffelbach, and T. Poinsot. Large Eddy Simulations of gaseous flames in gas turbine combustion chambers. *Progress in Energy and Combustion Science*, 38(6):782–817, December 2012.

[18] Peter Lax and Burton Wendroff. Systems of conservation laws. *Communications on Pure and Applied Mathematics*, 13(2):217–237, May 1960.

[19] J. Smagorinsky. General circulation experiments with the primitive equations. *Monthly weather review*, 91(3):99–164, 1963.

[20] J.-Ph. Legier, T. Poinsot, and D. Veynante. Dynamically thickened flame LES model for premixed and non-premixed turbulent combustion. In *Proceedings of the Summer Program*, pages 157–168, Stanford, 2000. Center for Turbulence Research.

[21] N. Noiray, D. Durox, T. Schuller, and S. Candel. A unified framework for nonlinear combustion instability analysis based on the flame describing function. *Journal of Fluid Mechanics*, 615:139, November 2008.

[22] A. Giauque, L. Selle, L. Gicquel, T. Poinsot, H. Buechner, P. Kaufmann, and W. Krebs. System identification of a large-scale swirled partially premixed combustor using LES and measurements. *Journal of Turbulence*, 6(February 2012):N21, January 2005.

[23] Luigi Crocco. Aspects of Combustion Stability in Liquid Propellant Rocket Motors Part I: Fundamentals. Low Frequency Instability With Monopropellants. *Journal of the American Rocket Society*, 21(6):163–178, November 1951.

[24] Luigi Crocco. Aspects of Combustion Stability in Liquid Propellant Rocket Motors Part II: Low Frequency Instability with Bipropellants. High Frequency Instability. *Journal of the American Rocket Society*, 22(1):7–16, January 1952.

[25] FE Marble and SM Candel. Acoustic disturbance from gas non-uniformities convected through a nozzle. *Journal of Sound and Vibration*, 55:225–243, 1977.

[26] P. Tucker, S. Menon, C. Merkle, J. Oefelein, and V. Yang. Validation of High-Fidelity CFD Simulations for Rocket Injector Design. In *44th AIAA/ASME/SAE/ASEE Joint Propulsion Conference and Exhibit*, pages AIAA–2008–5226, 2008.

[27] Matthew E. Harvazinski, William E. Anderson, and Charles L. Merkle. Analysis of Self-Excited Combustion Instabilities Using Two- and Three-Dimensional Simulations. *Journal of Propulsion and Power*, 29(2):396–409, March 2013.

[28] Fabrice Charlette, Charles Meneveau, and Denis Veynante. A power-law flame wrinkling model for LES of premixed turbulent combustion Part I: non-dynamic formulation and initial tests. *Combustion and Flame*, 131(1-2):159–180, October 2002.

[29] Thierry Poinsot, Arnaud C. Trouve, Denis Veynante, Sebastien M. Candel, and Emile Esposito. Vortex-driven acoustically coupled combustion instabilities. *J. Fluid Mech.* , 177:265–292, 1987.

[30] Konstantin I Matveev and FEC Culick. A model for combustion instability involving vortex shedding. *Combust. Sci. Tech.* , 175(6):1059–1083, 2003.